Desalination and Water Treatment
www.deswater.com
doi: 10.5004/dwt.2023.30151

316 (2023) 71–81
December

Improved bisphenol A degradation under visible-light irradiation through a $Bi_2Ti_2O_7$/g-C_3N_4 binary Z-scheme heterojunction

Dapeng Zhang[a,†], Xiaowei Xu[a,†], Zehua Zhao[a], Huihui Chen[b], Haifeng Tu[a], Jun Zhang[a], Cheng Zhang[a], Chaoyue Wu[a], Shanshan Su[a], Yang Lv[a], Jie Cao[a], Linli Liu[a], Yi Wang[a,*], Xiaochen Lin[a,*]

[a]*Nanjing Institute of Environmental Sciences, Ministry of Ecology and Environment of the People's Republic of China, 8 Jiangwangmiao Street, Nanjing 210042, China, emails: njtechwangyi@sina.com (Y. Wang), linxiaochen@nies.org (X. Lin)*
[b]*Shandong Resources and Environment Construction Group Co., Ltd., 2301G, Building 8, Shuntai Square, No. 2000, Shunhua Road, Hi-Tech Zone, Ji'nan 250101, China*

Received 2 September 2023; Accepted 20 November 2023

ABSTRACT

The photocatalytic degradation technique is considered to be one of the most promising approaches for solving the problem of environmental pollution. In this study, novel binary $Bi_2Ti_2O_7$/g-C_3N_4 Z-scheme heterojunctions were prepared using a calcination method. The prepared composite materials were used to degrade bisphenol A under visible-light irradiation. The degradation experiments proved that the composite material with 50 wt.% $Bi_2Ti_2O_7$ (denoted as BTC-50) showed excellent photocatalytic performance, which was consistent with the characterization results. The composite material displayed no significant decrease in photocatalytic activity after five recycles, and the degradation process was proven to follow pseudo-first-order kinetics. Besides, it was found that·O_2^- played the main role in the photocatalytic reaction process. This work significantly deepens the understanding of Z-scheme heterojunction material for organic degradation and provides ideas for the design of high-performance catalysts.

Keywords: g-C_3N_4; $Bi_2Ti_2O_7$; Bisphenol A; Photocatalyst; Heterojunction

1. Introduction

Bisphenol A (BPA) is a kind of organic compound with two phenol moieties with significant properties such as low vapor pressure, moderate water solubility, and low volatility. BPA is widely used in the manufacture of diverse containers and food packaging [1–3]. BPA is also a kind of endocrine disruptor, which can damage nerve cells, result in abnormal or disruptive behavior, and lead to heart disease, diabetes, and abnormalities in thyroid and liver functions [4,5].

It is reported that BPA at low concentration detected in surface water, industrial sewage, and domestic sewage has attracted scientists, the government, and even the common people's close attention [6]. Traditional disposal processes such as biodegradation, adsorption, coagulation, and membrane methods have been used for the removal of BPA despite having the drawbacks of no mineralization, low efficiency, sludge production, long reaction time, and phase transfer [7].

Photocatalysis process, with several advantages such as being environmentally friendly, highly efficient, and energy renewable, is widely used in the treatment of organic contaminants [8–10]. Photocatalysis mainly uses semiconductors and light irradiation to produce reactive oxygen species (ROS), such as superoxide (O_2^-) and hydroxyl radicals (OH). These ROS are powerful in mineralizing organics [11]. As is known, it is a key for the photocatalytic process

* Corresponding authors.
† These authors contributed equally to this work.

to find a suitable photocatalytic semiconductor [12–14]. Recently, as a kind of metal semiconductor photocatalytic material, bismuth titanates have aroused much attention owing to their excitation response under visible light, comparatively high dielectric constant, low dielectric loss, and small band gap to most ferroelectric perovskite oxides [15,16]. Bismuth titanates have a photocatalytic performance under visible light owing to the arrangement of Bi, 6p and O, 2p orbitals in the materials [17,18].

Bismuth titanates have the structure of mixed metal oxides and consist of a variety of phases such as $Bi_2Ti_2O_7$, $Bi_2Ti_4O_{11}$, $Bi_4Ti_3O_{12}$, $Bi_{12}TiO_{20}$, and $Bi_{20}TiO_{32}$ [19,20]. Oxide materials based on the pyrochlore structure compounds with general formula $A_2B_2O_7$ exhibit many physico-chemical and functional properties such as high dielectric permittivity, huge magnetoresistance, and photocatalytic activity. As a pyrochlore-type compound, bismuth titanate ($Bi_2Ti_2O_7$) was first synthesized in the 1960s [21,22]. $Bi_2Ti_2O_7$ has aroused widespread attention in recent years because of its unique crystal and electronic structure and possessing a low band-gap energy (approximately 2.6 eV) [14,23–25], whereas the efficiency of energy conversion is restricted by the fast recombination of photogenerated carriers of $Bi_2Ti_2O_7$ [20,23]. As reported, building heterojunctions with a suitable semiconductor is an effective strategy to address this issue. $Bi_2Ti_2O_7$-based heterojunction photocatalysts, such as $Bi_2Ti_2O_7/TiO_2$ [26], $BiVO_4/Bi_2Ti_2O_7$ [27], $Bi_2Ti_2O_7/Bi_4Ti_3O_{12}$ [28], $Bi_2Ti_2O_7/CaTiO_3$ [29], $Bi_2Ti_2O_7/TiO_2$/RGO [14], and $BiOCl/Bi_2Ti_2O_7$ [30], have been successfully prepared to enhance the photocatalytic performance. Moreover, doping a transition metal, such as Cr, Mn, Fe, Eu^{3+}, Er^{3+} and Yb^{3+} [31–33], to induce surface plasmon resonance also can further improve the recombination rate of photogenerated carriers.

In this work, graphitic carbon nitride (g-C_3N_4) was selected to combine with $Bi_2Ti_2O_7$ to form heterojunction due to its remarkable properties, such as suitable bandgap (2.7 eV), high thermal and chemical stability, visible light response, and environmental friendly [34,35]. $Bi_2Ti_2O_7$ and g-C_3N_4 were prepared via calcination and solvothermal methods, respectively. The two materials were combined to synthesize $Bi_2Ti_2O_7$/g-C_3N_4 Z-scheme heterojunctions. Characterizations such as morphological analysis, crystal structure analysis, and photoelectric properties analysis were performed. Moreover, BPA was selected as the target contaminant to investigate the prepared $Bi_2Ti_2O_7$/g-C_3N_4 Z-scheme heterojunctions. The possible degradation mechanism of $Bi_2Ti_2O_7$/g-C_3N_4 was also considered, based on the energy band theory.

2. Experimental set-up

2.1. Chemicals

Melamine (AR) and BPA (AR) were purchased from Sinopharm Chemical Reagent Company (Shanghai, China). Absolute ethyl alcohol (AR), tetrabutyl titanate (AR), absolute ether (AR), *p*-benzoquinone (AR), isopropanol (AR), and potassium iodide (AR) were obtained from Shanghai Chemical Reagent Company (Shanghai, China). Purified water (Wahaha Group Ltd., Hangzhou, China) was used throughout the experiments. All chemicals were used without further purification.

2.2. Apparatus

The morphology and structure of g-C_3N_4, $Bi_2Ti_2O_7$, and $Bi_2Ti_2O_7$/g-C_3N_4 Z-scheme heterojunctions were studied using transmission electron microscopy (TEM, JEM-200CX microscope, JEOL, Tokyo, Japan) and a scanning electron microscope (SEM, Hitachi-S4800, Tokyo, Japan). Fourier-transform infrared spectroscopy (FTIR) was recorded on a TENSOR 27 spectrometer using a potassium bromide pellet (Bruker, Saarbrucken, Germany). The phase purity and crystallinity of the as-prepared materials were identified from X-ray powder diffraction (XRD) patterns on a Rigaku XRD-6000 diffractometer with Cu Kα radiation (λ = 0.15406 nm) (Shimadzu, Kyoto, Japan). X-ray photoelectron spectroscopy (XPS) data were obtained on an Escalab 250Xi instrument (Thermo, USA). The ultraviolet-visible diffuse reflectance spectroscopy (UV-Vis DRS) was performed with a Cary 5000 spectrophotometer in the 200–800 nm range and $BaSO_4$ was chosen as the reference (Varian, USA). A Cary Eclipse spectrophotometer (Varian, USA) was employed for photoluminescence (PL) analysis.

2.3. Preparation of the photocatalytic materials

2.3.1. Preparation of g-C_3N_4

The g-C_3N_4 nanosheets were prepared by the calcination method with minor modifications [36]. Melamine (30 g) was calcined in a tube furnace at 520°C for 4 h under an air atmosphere. The yellow solid obtained is g-C_3N_4.

2.3.2. Preparation of $Bi_2Ti_2O_7$

$Bi_2Ti_2O_7$ particles were synthesized via the solvothermal method [37,38]. In brief, 0.8537 g $Bi(NO_3)_3{\cdot}5H_2O$, 18 mL absolute ethyl alcohol, and 7 mL glycerol were dispersed in a Teflon-lined stainless-steel autoclave. Then, 1.5 mL tetrabutyl titanate was slowly added to the mixed system with ultrasound irradiation. Absolute ether (5 mL) was added when the solid matter was dissolved. The mixture was digested at 110°C for 12 h. After the reaction, the obtained samples were centrifugally washed and dried and then calcined in a tubular furnace at 500°C for 3 h. $Bi_2Ti_2O_7$ was obtained after cooling to room temperature.

2.3.3. Preparation of $Bi_2Ti_2O_7$/g-C_3N_4

Distinguishing from the synthesis process of pure $Bi_2Ti_2O_7$, a certain amount of g-C_3N_4 was dispersed in the mixed solvent with 18 mL absolute ethyl alcohol and 7 mL glycerol. The rest of the synthesis process was the same as that of $Bi_2Ti_2O_7$. Different proportions of $Bi_2Ti_2O_7$ (70%, 50%, and 30%) in $Bi_2Ti_2O_7$/g-C_3N_4 composite materials were obtained by changing the dosing of g-C_3N_4, and they were labeled BTC-70, BTC-50, and BTC-30, respectively.

3. Results and discussion

3.1. Characterization of the prepared materials

3.1.1. Morphology analysis

The morphology and structure of $Bi_2Ti_2O_7$/g-C_3N_4 were observed via TEM and SEM. Fig. 1a shows that single

g-C_3N_4 had a lamellar structure, which is consistent [39,40]. As shown in Fig. 1b $Bi_2Ti_2O_7$ had a spherical-like structure. Fig. 1c–f show that g-C_3N_4 was successfully loaded on the surface of $Bi_2Ti_2O_7$. Fig. 1d displays the lattice fringes of BTC-50 had a spacing of 0.298 and 0.235 nm, which are in accord with the spacing of the (444) and (662) planes of $Bi_2Ti_2O_7$. The heterojunctions of BTC-30, BTC-50 and BTC-70 can be clearly observed in high-resolution transmission electron microscopy (HRTEM) images (Fig. 1c~e). Compared with HRTEM images of BTC-30 and BTC-70 (Fig. 1c and e), more heterojunctions can be observed in that of BTC-50, which is more beneficial to decrease the recombination probability of electron and hole and provide more photocatalytic active sites.

3.1.2. FTIR analysis

Fig. 2a shows peaks at 1,253 and 1,644 cm^{-1} that result from the stretching vibrations of C–N and C=N [41], respectively. The wide peaks at 3,100–3,400 cm^{-1} were ascribed to the $–NH_2$ group [42,43]. The peak at 803 cm^{-1} corresponded to the breathing of the triazine units of g-C_3N_4 [41–43]. The two characteristic peaks at 563 and 758 cm^{-1} were assigned to the stretching vibrations of Ti–O and Bi–O bonds, respectively [14]. The absorption band that appeared at 920 cm^{-1} represented the Ti–O stretching of the octahedral TiO_6 group [15]. All the typical characteristic peaks such as 1,644 and 803 cm^{-1} of g-C_3N_4 and 563 and 920 cm^{-1} of $Bi_2Ti_2O_7$ were contained in the binary BTC composites (Fig. 2c–e), which confirmed the successful synthesis of the composite materials.

3.1.3. XRD analysis

The XRD analysis is shown in Fig. 3. The intense peaks at 13.15° and 27.50° correspond to the (100) and (002) planes of g-C_3N_4, respectively [44]. The two peaks resulted from the characteristic interplanar stacking of the aromatic systems [45,46]. Fig. 3b shows the characteristic diffraction peaks of $Bi_2Ti_2O_7$ were at 11.83°, 14.80°, 27.06°, 28.86°, 29.85°, 32.37°, 34.59°, 37.83°, 45.49°, 48.08°, 49.77°, 52.19°, 56.86°, 59.15°, 62.11°, 73.21°, 80.96°, and 81.54°, which were indexed as

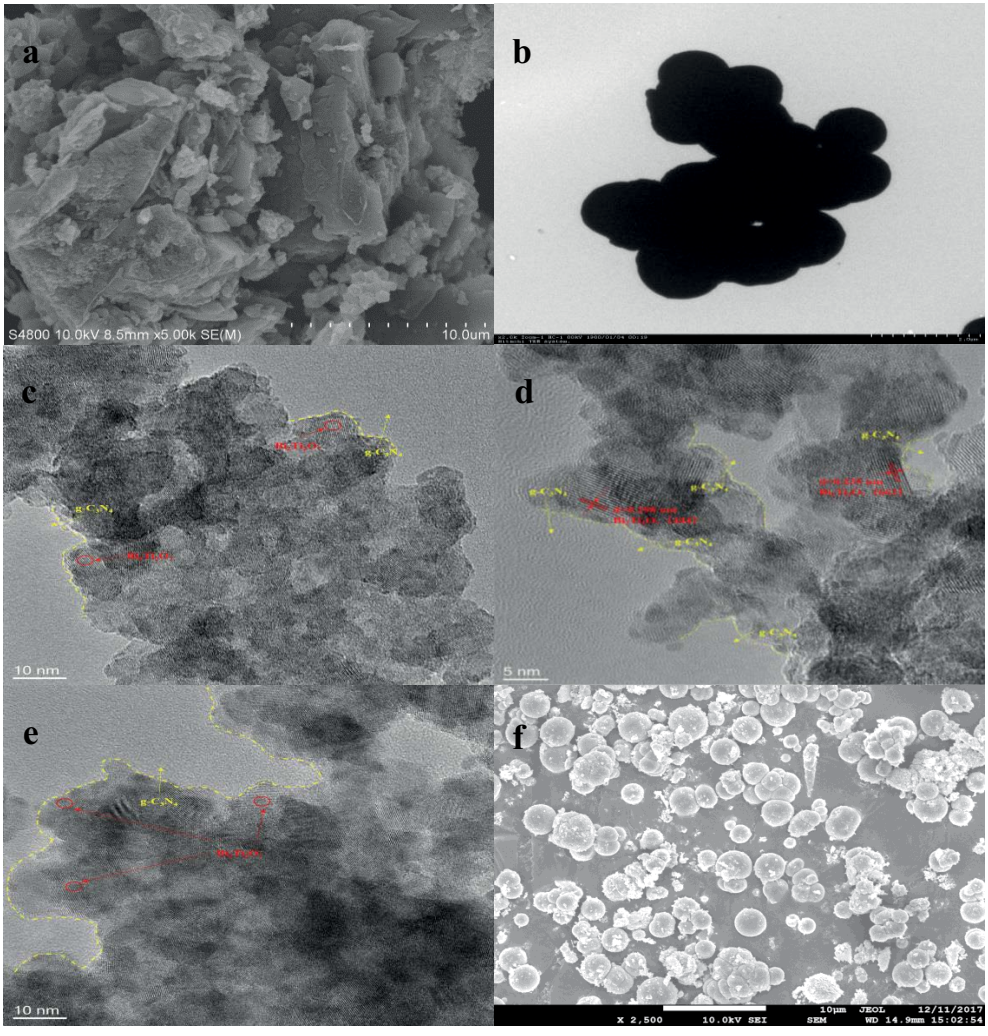

Fig. 1. Scanning electron microscopy images of g-C_3N_4 (a) and BTC-50 (f), transmission electron microscopy image of $Bi_2Ti_2O_7$ (b), high-resolution transmission electron microscopy images BTC-30 (c), BTC-50 (d) and BTC-70 (e).

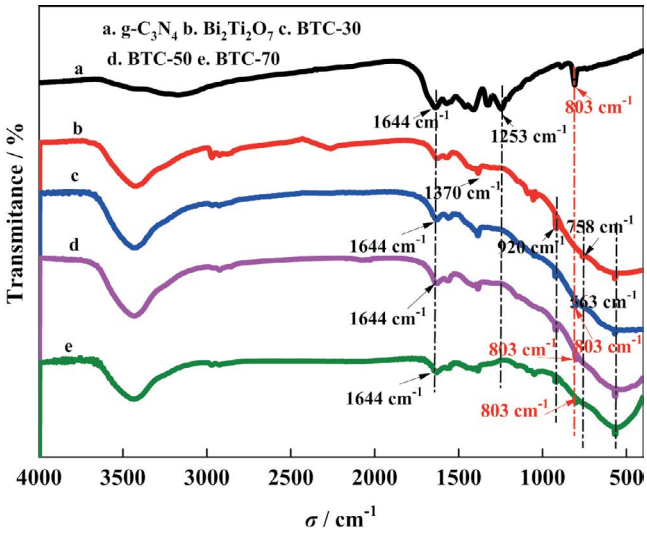

Fig. 2. Fourier-transform infrared spectra of g-C_3N_4 (a), $Bi_2Ti_2O_7$ (b), BTC-30 (c), BTC-50 (d) and BTC-70 (e).

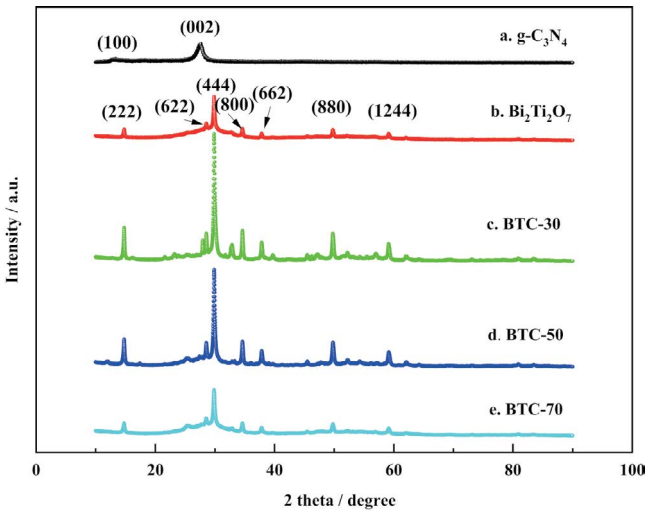

Fig. 3. X-ray powder diffraction spectra of g-C_3N_4 (a), $Bi_2Ti_2O_7$ (b), BTC-30 (c), BTC-50 (d) and BTC-70 (e).

the (220), (222), (620), (622), (444), (642), (800), (662), (1022), (1042), (880), (1062), (1153), (1244), (888), (1600), (14102), and (12124) crystal planes of $Bi_2Ti_2O_7$. These intense peaks can be observed in JCPDS Card No. 32-0118 [28,29]. All the diffraction peaks of g-C_3N_4 and $Bi_2Ti_2O_7$ can be seen in Fig. 3c–e, which confirmed the BTC composites were successfully prepared.

3.1.4. XPS analysis

XPS was used to characterize the inner structure of BTC-50 composite material. According to the full scan spectrum in Fig. 4a, the elements C, N, O, Ti, and Bi can be observed in the BTC-50 composite material. In C 1s (Fig. 4b), the double peaks at 288.0 eV and 287.2 eV resulted from the C–$(N)_3$ in g-C_3N_4. The peak at 284.7 eV corresponded to the C–C bonding in graphitic or amorphous carbon in the nanocomposite [47,48]. The two N 1s peaks at 397.6 and 398.4 eV were ascribed to the bonds of N–C–N and C=N–C (Fig. 4c) [49], which demonstrated the presence of g-C_3N_4 in BTC-50. According to Fig. 4d, the binding energy of O 1s corresponded to the two characteristic peaks at 530.3 and 531.6 eV, indicating the existence of Bi–O and Ti–O [50]. In Fig. 4e, the intense double peaks at 159.4 and 164.6 eV were connected with the binding energies of Bi $4f_{7/2}$ and Bi $4f_{5/2}$, respectively, which showed the existence of Bi^{3+} [50–52]. The two peaks at 466.3 and 464.5 eV were relevant to the binding energy of Ti $2p_{1/2}$. The peak at 458.7 eV was ascribed to Ti $2p_{3/2}$ (Fig. 4f) [50,53–54].

3.1.5. DRS analysis

The light absorption performance of catalytic materials plays a crucial role in photocatalytic performance. The UV-Vis DRS was utilized to study the light absorption performance of g-C_3N_4, $Bi_2Ti_2O_7$, and BTC-50 composite material (Fig. 5). As shown in Fig. 5a, the basic absorption edge of g-C_3N_4 was at about 460 nm [55,56], whereas the $Bi_2Ti_2O_7$ had obvious light absorption at nearly 450 nm [50]. Compared with the two single materials, the light absorption intensity of BTC-50 composite material was slightly improved. Fig. 5b shows that the band gaps (E_g) of g-C_3N_4 and $Bi_2Ti_2O_7$ were 2.70 and 2.60 eV, respectively.

3.1.6. PL analysis

To compare the generation and separation of photogenic carriers of pure g-C_3N_4, $Bi_2Ti_2O_7$, and BTC-50, fluorescence intensity was utilized with an excitation wavelength of 260 nm. Fig. 6 shows g-C_3N_4 had the highest fluorescence intensity, which was followed by $Bi_2Ti_2O_7$ and BTC-50. The result confirmed the heterojunction in the prepared composite material promotes the separation of photoinduced carriers.

3.2. Photocatalytic degradation of BPA

3.2.1. Effect of the component ratio of $Bi_2Ti_2O_7$/g-C_3N_4 on the degradation of BPA

Different photocatalytic materials (15 mg) were added to 50 mL 10 mg/L BPA solutions (Fig. 7). Compared with composite catalysts (BTC), both single g-C_3N_4 and $Bi_2Ti_2O_7$ had lower degradation efficiency of BPA after 300 min visible-light irradiation. BTC composite catalysts exhibited obviously improved photocatalytic performance. Moreover, it was worth noting that BTC-50 showed the optimal photocatalytic performance, which resulted from the effective electron migration from BTC-50 composite material. Hence, BTC-50 nanomaterial was used in the following experiments.

3.2.2. Effect of salinity on the degradation of BPA

Fig. 8 shows that the degradation efficiency of BPA was negatively correlated with NaCl concentration. BPA degradation efficiency only reached 70% when the dosage

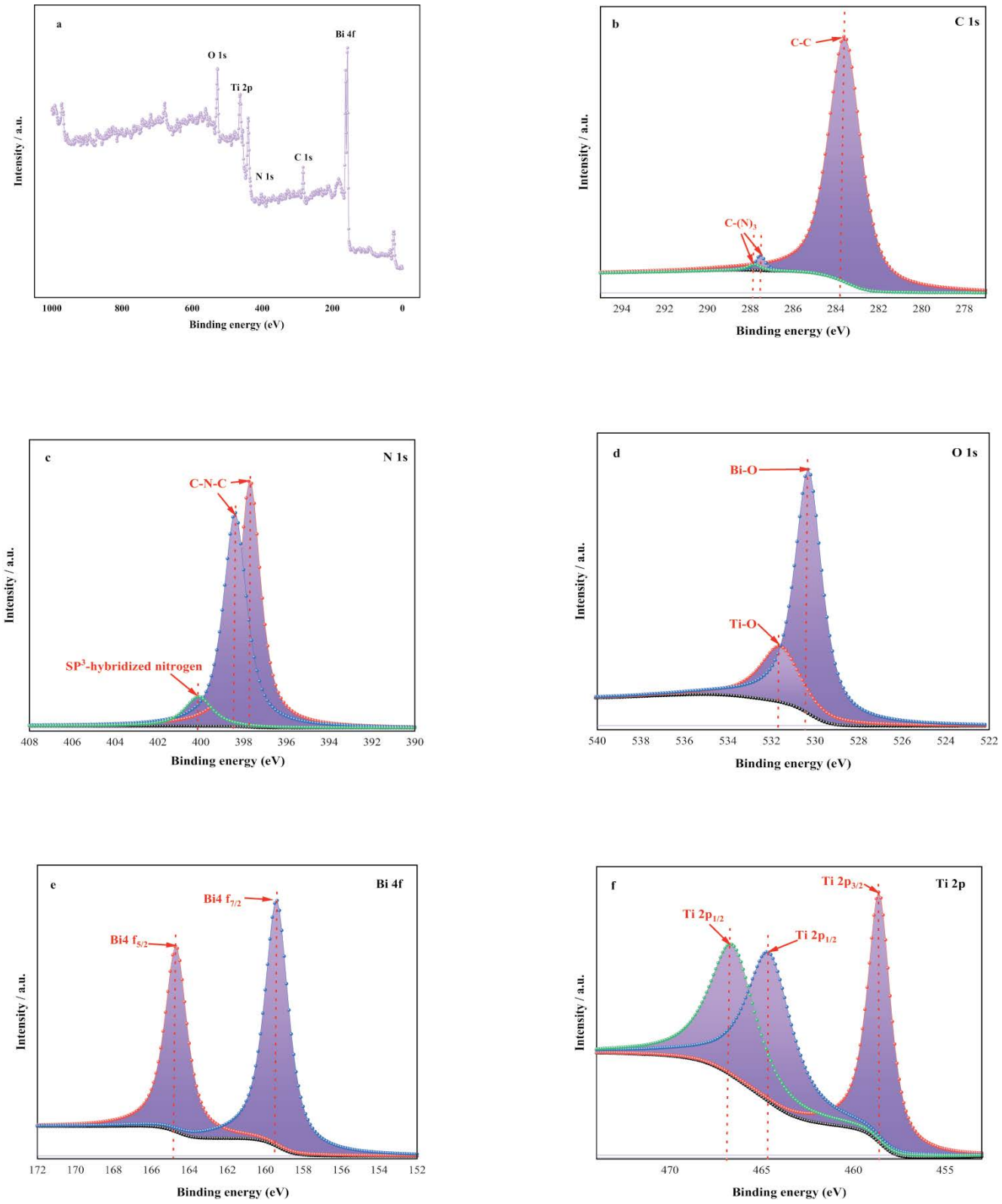

Fig. 4. X-ray photoelectron spectra of C, N, O, Bi and Ti elements in BTC-50.

of NaCl was 0.9%. It may probably be due to the occupation of Na^+ on the reactive sites in the BTC-50 composite material, which prohibited the BPA molecules from adsorbing onto the composite surface [57]. Besides, competitive adsorption among Cl^-, OH^-, and electrons would occur on the surface of BTC-50. Fig. 9 shows that the

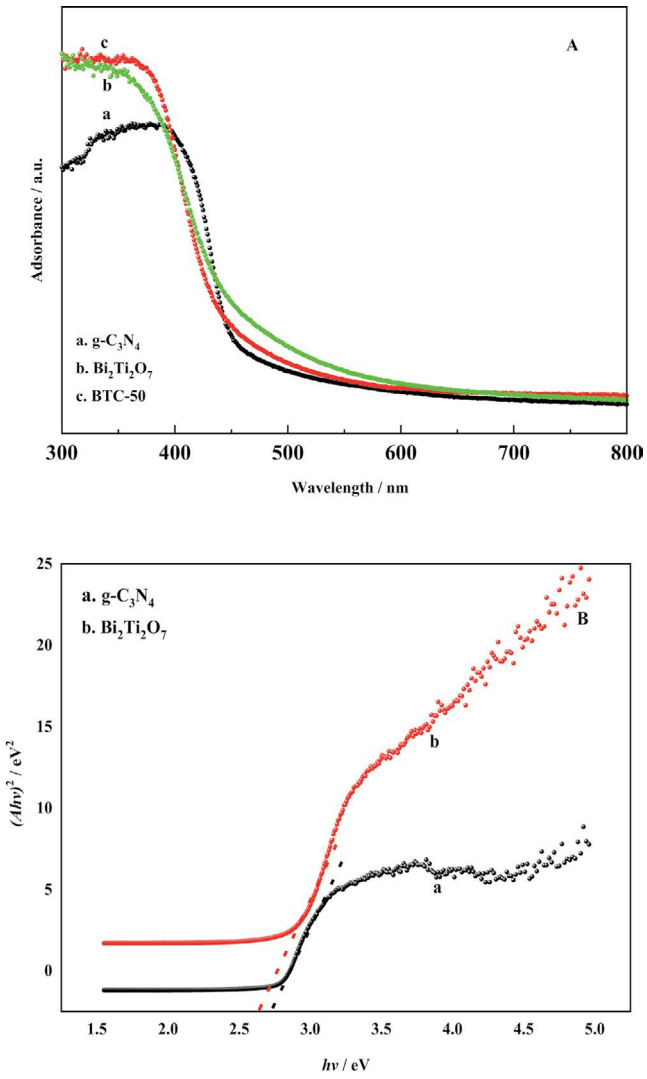

Fig. 5. Diffuse reflectance spectra of g-C_3N_4, $Bi_2Ti_2O_7$ and BTC-50.

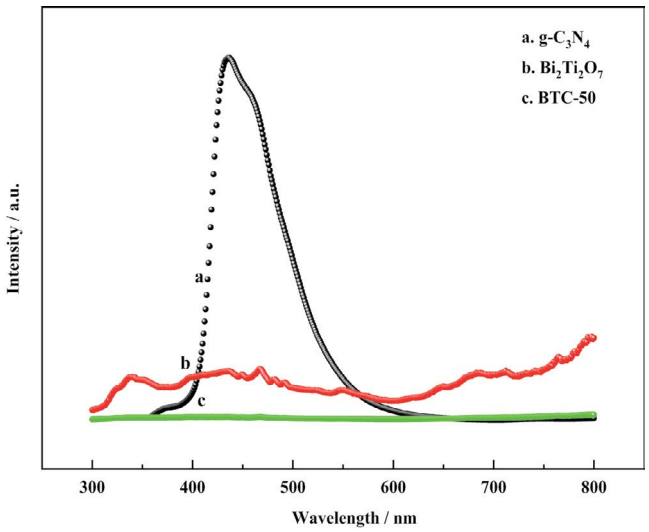

Fig. 6. Photoluminescence spectra of g-C_3N_4 (a), $Bi_2Ti_2O_7$ (b) and BTC-50 (c).

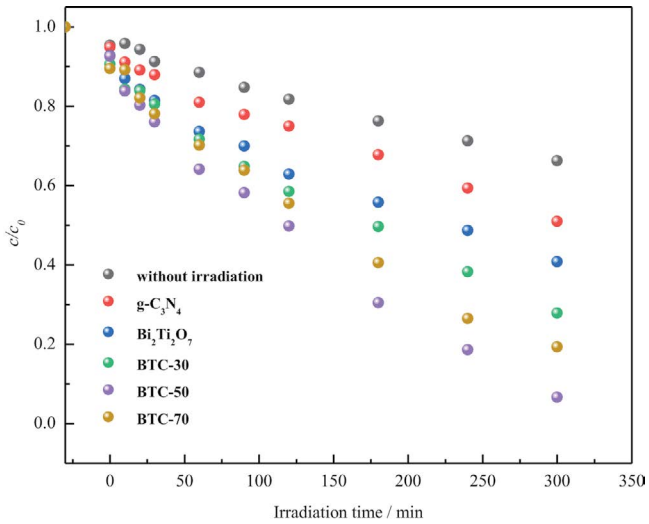

Fig. 7. Effect of the component ratio of BTC nanocomposites on the degradation efficiency (BPA = 10 mg/L, catalysis = 10 mg, pH = 7).

degradation process obeys pseudo-first-order kinetics because of the linear relationship between $\ln(C_0/C)$ and reaction time (Eq. (1)).

$$\ln\left(\frac{C_0}{C}\right) = kt \tag{1}$$

where C_0 is the initial concentration of BPA (units: mg/L) and C is the concentration of BPA after the photocatalytic reaction (units: mg/L), t is the irradiation time (min), k is the reaction rate constant (min^{-1}).

Fig. 10a shows Rhodamine B (RhB) degradation efficiency of this material with ABC-50 [55] and APC-25 [36]. The degradation efficiency of RhB was a little less than that ABC-50 and APC-25, which may due to the difference of pore size of materials and the size of molecular. As shown in Fig. 10b, the photocatalytic degradation was studied under actual water sample including Yangtze River, Xuanwu Lake, tap water in Nanjing, and the East China Sea, which were all spiked with 10 mg/L BPA. The degradation efficiency differs from 74.32% to 84.11%, which were a little less than that in pure water (93.32%). It may be related to the salinity and solution pH in the real water.

3.2.3. Reusability of the composite catalyst

Catalyst stability is very important for practical applications. The cycle experiment results are in Fig. 11, the degradation efficiency can still reached 90% after five recycles. The photocatalytic activity had only a slight decrease, which showed the prepared composite catalyst had satisfactory stability of the heterojunction structure and photocatalytic activity.

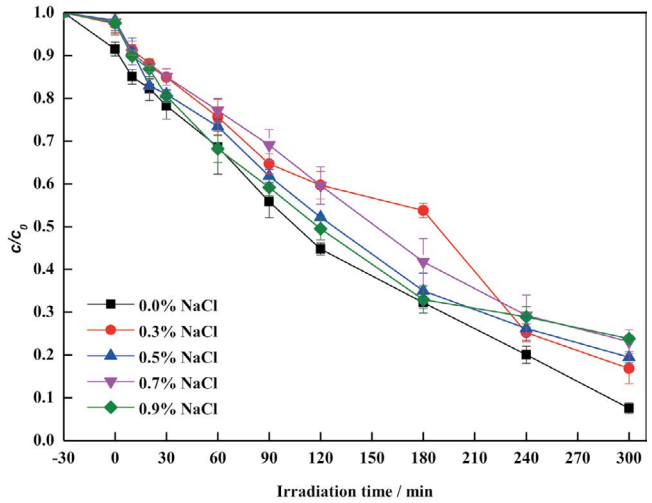

Fig. 8. Effect of the salinity of degradation efficiency of BPA (BPA = 10 mg/L, catalysis = 10 mg, pH = 7).

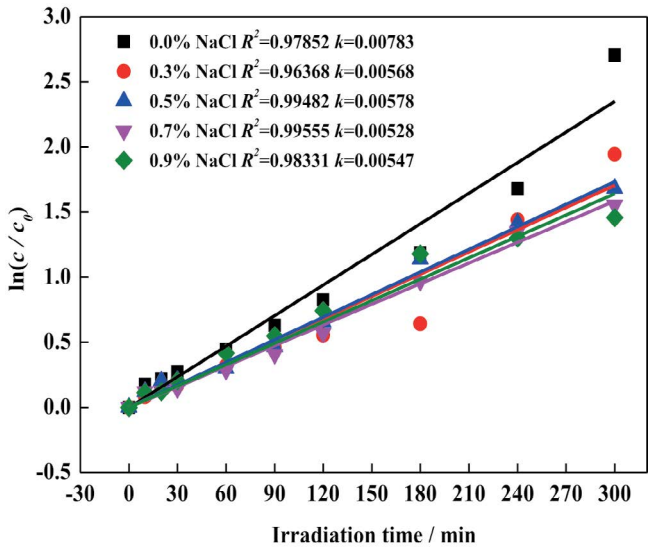

Fig. 9. First-order kinetics simulation diagram of BPA degradation.

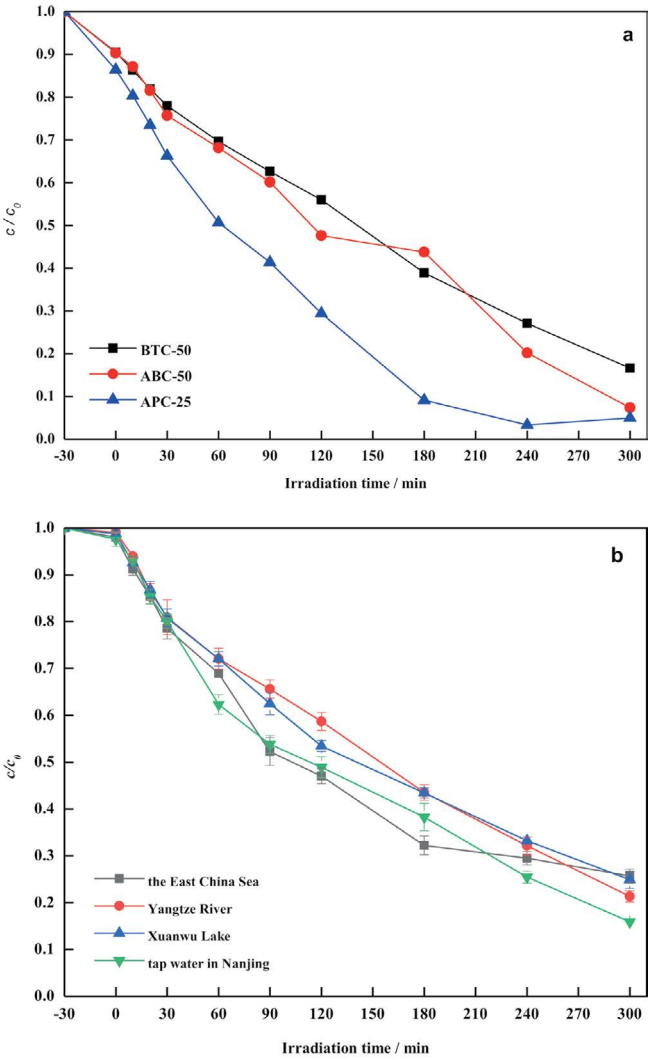

Fig. 10. (a) Rhodamine B degradation efficiency of this material with ABC-50 and APC-25 (pH = 7, catalyst = 10 mg, RhB = 10 mg/L) and (b) photocatalytic degradation under actual water sample including Yangtze River, Xuanwu Lake, tap water in Nanjing, and the East China Sea (pH = 7, catalyst = 10 mg, BPA = 10 mg/L).

3.3. Possible photocatalytic mechanism

Active free radicals play a significant role during the photocatalytic degradation process. To determine the main active substances in BPA degradation by BTC-50, 10 mmol/L isopropanol, potassium iodide, and *p*-benzoquinone were employed as scavengers for •OH, h^+, and $•O_2^-$, respectively. The experimental results are shown in Fig. 12. The rate constants (k) of three photocatalytic degradation processes with the corresponding scavengers are 0.00582 min^{-1} (potassium iodide), 0.00574 min^{-1} (isopropanol), and 0.00194 min^{-1} (*p*-benzoquinone). The k of the degradation system with *p*-benzoquinone was the lowest, which verified that $•O_2^-$ makes a prominent contribution to BPA degradation by BTC-50.

In our previous work, the E_{CB} values and E_{VB} values of g-C_3N_4 were measured as –1.13 and 1.57 eV, respectively [36,55,58]. The E_{CB} values and E_{VB} values of $Bi_2Ti_2O_7$ were calculated using Mulliken electronegativity theory [Eqs. (2) and (3)].

$$E_{VB} = X - E_C + 0.5E_g \quad (2)$$

$$E_{CB} = E_{VB} - E_g \quad (3)$$

where X is the absolute electronegativity of a semiconductor (X-$Bi_2Ti_2O_7$ = 5.95 eV); E_C is the energy of free electrons vs hydrogen (4.5 eV) [59]. According to Eqs. (1) and (2), the values of E_{CB} and E_{VB} for $Bi_2Ti_2O_7$ are predicted to be 0.15 and 2.75 eV, respectively.

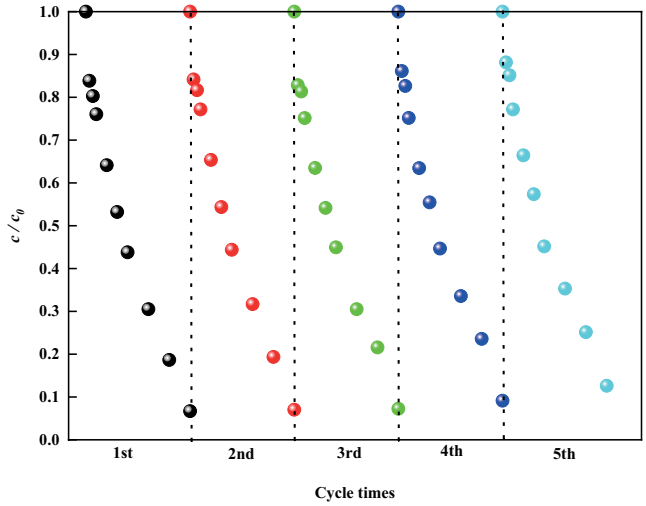

Fig. 11. Effect of reborn BTC-50 on the degradation efficiency of BPA.

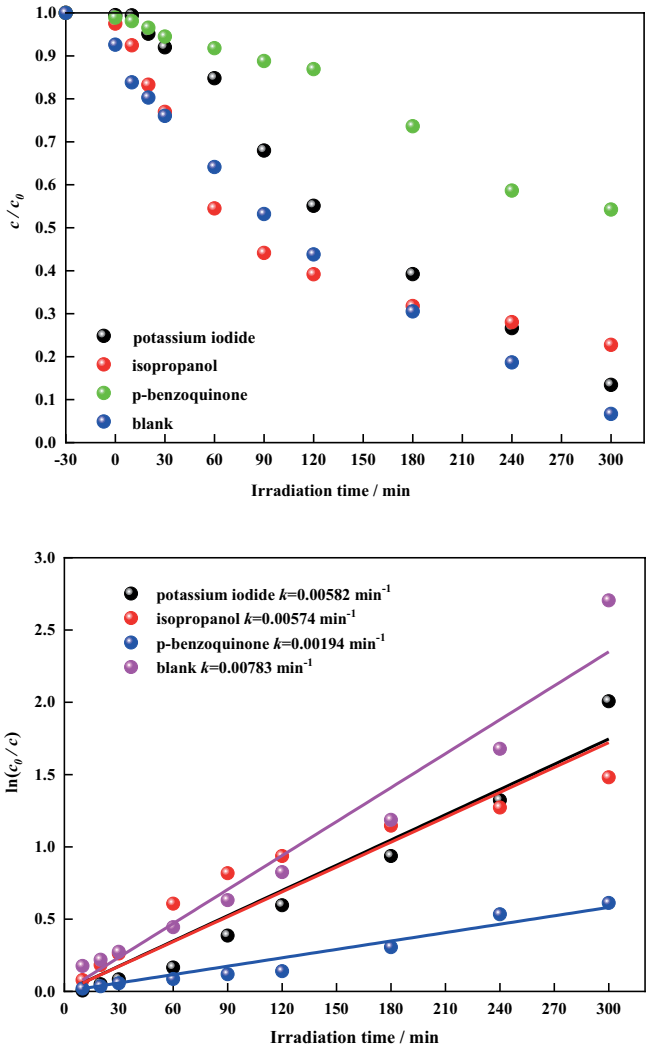

Fig. 12. Effects of trapping agents on the degradation efficiency and rate constant of BPA.

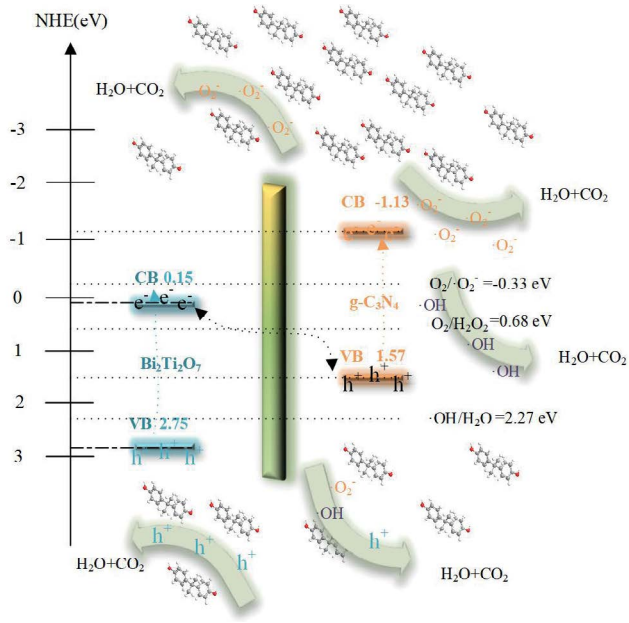

Fig. 13. Schematic drawing of the photocatalytic degradation of the BTC-50 nanocomposite.

Based on the E_{CB} and E_{VB} positions of g-C_3N_4 and $Bi_2Ti_2O_7$ and the energy band theory, a possible photocatalytic mechanism for BTC-50 binary composite material can be proposed. The photogenerated e^- of g-C_3N_4 and $Bi_2Ti_2O_7$ could migrate from the valence band (VB) to the corresponding conduction band (CB) under visible-light irradiation and h^+ are generated and remain in the VB. Because the gap between the VB of g-C_3N_4 and CB of $Bi_2Ti_2O_7$ is relatively small, e^- in the CB of $Bi_2Ti_2O_7$ is easier to recombine with h^+ in the VB of g-C_3N_4. Hence, e^- are stored in the CB of g-C_3N_4, while h^+ are stored in the VB of $Bi_2Ti_2O_7$ for the whole BTC-50 binary composite material. Because the CB potential of g-C_3N_4 is more negative than that of $O_2/{}^{\bullet}O_2^-$ ($O_2/{}^{\bullet}O_2^-$ = –0.33 eV) [60], the e^- in the CB of g-C_3N_4 can react with dissolved O_2 in water to generate ${}^{\bullet}O_2^-$. Then, ${}^{\bullet}O_2^-$ can directly oxidize the target organic pollutant. Furthermore, ${}^{\bullet}O_2^-$ can combine with H^+ in water to produce H_2O_2 (O_2/H_2O_2 = +0.68 eV) [61], which can further turn into ${}^{\bullet}OH$. Because the VB potential of $Bi_2Ti_2O_7$ (+2.75 eV) is more positive than that of ${}^{\bullet}OH/H_2O$ (${}^{\bullet}OH/H_2O$ = +2.27 eV) [62], h^+ in the VB of $Bi_2Ti_2O_7$ could directly react with H_2O to generate ${}^{\bullet}OH$, which also can degrade organic matter. Moreover, the oxidation abilities of holes can be used to mineralize and decompose the organic contaminant.

Combined with the above analysis, the possible photocatalytic process mechanism and analogue diagram are proposed as shown in Eqs. (4)–(8) and Fig. 13.

$$BTC-50+hv\rightarrow e^-+h^+ \quad (4)$$

$$O_2+e^-\rightarrow {}^{\bullet}O_2^- \quad (5)$$

$$2{}^{\bullet}O_2^-+2H^+\rightarrow 2{}^{\bullet}OH+O_2 \quad (6)$$

$$H_2O+h^+\rightarrow {}^{\bullet}OH+H^+ \quad (7)$$

$$^{\bullet}O_2^-/^{\cdot}OH/h^+ + BPA \rightarrow CO_2 + H_2O \quad (8)$$

4. Conclusions

Herein, $Bi_2Ti_2O_7$/g-C_3N_4 composite catalysts were successfully synthesized. TEM/SEM, XRD, FTIR, XPS, DRS, and PL were used to characterize the structure. The degradation experiment of bisphenol A showed the 50 wt.% $Bi_2Ti_2O_7$/g-C_3N_4 exhibited the highest efficiency of 93.32% for the photo-degradation of bisphenol A after 300 min visible-light irradiation. The prepared composite catalyst had satisfactory stability and photocatalytic activity after five recycles. The photocatalytic process kinetics and a possible reaction mechanism were also suggested. The degradation process was shown to follow pseudo-first-order kinetics. The order of the oxidation efficiency toward BPA is $^{\bullet}O_2^-$ > $^{\bullet}OH$ > h^+. This study provides a novel solution strategy to the phenolic pollutant's degradation in actual wastewater by the construction of bismuth-based Z-scheme heterojunction.

Acknowledgement

This work was financially supported by Jiangsu Postdoctoral Research Funding Program (Grant no. 2021K234B). We thank International Science Editing (http://www.internationalscienceediting.com) for editing this manuscript.

References

[1] K. Czarny, B. Krawczyk, D. Szczukocki, Toxic effects of bisphenol A and its analogues on cyanobacteria *Anabaena variabilis* and *Microcystis aeruginosa*, Chemosphere, 263 (2021) 128299, doi: 10.1016/j.chemosphere.2020.128299.

[2] J.J. Wang, J.N. Yu, Y. Yu, Z.S. Luo, G.F. Li, X.Y. Lin, Nanoporous electrode with stable polydimethylsiloxane coating for direct electrochemical analysis of bisphenol A in complex wine media, Food Chem., 405 (2023) 134806, doi: 10.1016/j.foodchem.2022.134806.

[3] K. Czarny-Krzymińska, B. Krawczyk, D. Szczukocki, Bisphenol A and its substitutes in the aquatic environment: occurrence and toxicity assessment, Chemosphere, 315 (2023) 137763, doi: 10.1016/j.chemosphere.2023.137763.

[4] R.X. Ma, J.X. Jiang, Y.F. Ya, Y. Lin, Y.Y. Zhou, Y.Y. Wu, X.C. Tan, K.J. Huang, F.K. Du, J.J. Xu, A carbon dot-based nanoscale covalent organic framework as a new emitter combined with a CRISPR/Cas12a-mediated electrochemiluminescence biosensor for ultrasensitive detection of bisphenol A, Analyst, 146 (2023) 1362–1370.

[5] S.J. Singh, A. Tandon, Phoolmala, T. Srivastava, N. Singh, S. Goyal, S. Priya, R.K. Chaturvedi, Mol, Bisphenol-A (BPA) impairs *Hippocampal neurogenesis via* inhibiting regulation of the ubiquitin proteasomal system, Mol. Neurobiol., 60 (2023) 3277–3298.

[6] H.Y. Yu, W.L. Song, X. Chen, Q. Zhao, X.X. Du, Transcriptomic analysis reveals up-regulated histone genes may play a key role in zebrafish embryo-larvae response to Bisphenol A (BPA) exposure, Ecotoxicol. Environ. Saf., 252 (2023) 114578, doi: 10.1016/j.ecoenv.2023.114578.

[7] A. Hassani, P. Eghbali, F. Mahdipour, S. Wacławek, K.Y.A. Lin, F. Ghanbari, Insights into the synergistic role of photocatalytic activation of peroxymonosulfate by UVA-LED irradiation over $CoFe_2O_4$-rGO nanocomposite towards effective Bisphenol A degradation: performance, mineralization, and activation mechanism, Chem. Eng. J., 453 (2023) 139556, doi: 10.1016/j.cej.2022.139556.

[8] C.P. Gao, G. Liu, X.M. Liu, X.Y Wang, M.M. Liu, Y.L. Chen, X. Jiang, G.X. Wang, Z.C. Teng, W.L Yang, Flower-like n-Bi_2O_3/n-BiOCl heterojunction with excellent photocatalytic performance for visible light degradation of Bisphenol A and Methylene blue, J. Alloys Compd., 929 (2022) 167296, doi: 10.1016/j.jallcom.2022.167296.

[9] X.H. Wang, W.W. Tang, L.B. Jiang, J. Feng, J.J. Yang, S.Y. Zhou, W.Q. Li, X.Z. Yuan, H. Wang, J.J. Wang, Y.Q. Bu, Mechanism insights into visible light-induced crystalline carbon nitride activating periodate for highly efficient ciprofloxacin removal, Chem. Eng. J., 471 (2023) 144521, doi: 10.1016/j.cej.2023.144521.

[10] S.Y. Zhou, L.B. Jiang, H. Wang, J.J. Yang, X.Z. Yuan, H. Wang, J. Liang, X.D. Li, H. Li, Y.Q. Bu, Oxygen vacancies modified TiO_2/O-terminated Ti_3C_2 composites: unravelling the dual effects between oxygen vacancy and high-work-function titanium carbide, Adv. Funct. Mater., 33 (2023) 2307702, doi: 10.1002/adfm.202307702.

[11] A. Iqbal, F.B. Shittu, M.N.M. Ibrahim, N.H.H. Abu Bakar, N. Yahaya, K. Rajappan, M.H. Hussin, W.H. Danial, L.D. Wilson, Photoreactive carbon dots modified g-C_3N_4 for effective photooxidation of bisphenol-a under visible light irradiation, Catalysts, 12 (2022) 1311, doi: 10.3390/catal12111311.

[12] X.M. Gu, T.J. Chen, J. Lei, Y. Yang, X.Z. Zheng, S.J. Zhang, Q.S. Zhu, X.L. Fu, S.G. Meng, S.F. Chen, Self-assembly synthesis of S-scheme g-C_3N_4/$Bi_8(CrO_4)O_{11}$ for photocatalytic degradation of norfloxacin and bisphenol A, Chin. J. Catal., 43 (2022) 2569–2580.

[13] Y.F. Li, M.H. Zhou, B. Cheng, Y. Shao, Recent advances in g-C_3N_4-based heterojunction photocatalysts, J. Mater. Sci. Technol., 56 (2020) 1–17.

[14] W.G. Li, Y.J. Zuo, L. Jiang, D.C. Yao, Z.J. Chen, G.Y. He, H.Q. Chen, $Bi_2Ti_2O_7$/TiO_2/RGO composite for the simulated sunlight-driven photocatalytic degradation of ciprofloxacin, Mater. Chem. Phys., 256 (2020) 123650, doi: 10.1016/j.matchemphys.2020.123650.

[15] A.K. Yadav, A. Gaur, K.K. Haldar, Effect of oxygen vacancies, lattice distortions and secondary phase on the structural, optical, dielectric and ferroelectric properties in Cd-doped $Bi_2Ti_2O_7$ nanoparticles, Mater. Res. Bull., 141 (2021) 111373, doi: 10.1016/j.materresbull.2021.111373.

[16] Y. Naciri, A. Hsini, A. Ahdour, B. Akhsassi, K. Fritah, Z. Ajmal, R. Djellabi, A. Bouziani, A. Taoufyq, B. Bakiz, A. Benlhachemi, M. Sillanpää, H.T. Li, Recent advances of bismuth titanate based photocatalysts engineering for enhanced organic contaminates oxidation in water: a review, Chemosphere, 300 (2022) 134622, doi: 10.1016/j.chemosphere.2022.134622.

[17] G.A. Kallawar, D.P. Barai, B.A. Bhanvase, Bismuth titanate based photocatalysts for degradation of persistent organic compounds in wastewater: a comprehensive review on synthesis methods, performance as photocatalyst and challenges, J. Cleaner Prod., 318 (2021) 128563, doi: 10.1016/j.jclepro.2021.128563.

[18] S.T.U. Din, W.F. Xie, W.C. Yang, Synthesis of Co_3O_4 nanoparticles-decorated $Bi_{12}O_{17}Cl_2$ hierarchical microspheres for enhanced photocatalytic degradation of RhB and BPA, Int. J. Mol. Sci., 23 (2022) 15028, doi: 10.3390/ijms232315028.

[19] L.D. Kong, H.H. Chen, W.M. Hua, S.C. Zhang, J.M. Chen, Mesoporous bismuth titanate with visible-light photocatalytic activity, Chem. Commun., 40 (2008) 4977–4979.

[20] D. Zhou, H. Yang, Y.F. Tu, Y. Tian, Y.X. Cai, Z.L. Hu, X.L. Zhu, *In-situ* fabrication of $Bi_2Ti_2O_7$/TiO_2 heterostructure submicron fibers for enhanced photocatalytic activity, Nanoscale Res. Lett., 11 (2016) 193, doi: 10.1186/s11671-016-1408-7.

[21] N.A. Lomanova, M.V. Tomkovich, V.V. Sokolov, Ugolkov, V.L. Ugolkov, Formation and thermal behavior of nanocrystalline $Bi_2Ti_2O_7$, Russ. J. Gen. Chem., 88 (2018) 2459–2464.

[22] A.A. Bush, M.V. Talanov, A.I. Stash, S.A. Ivanov, K.E. Kamentsev, Relaxor-like behavior and structure features of $Bi_2Ti_2O_7$ pyrochlore single crystals, Cryst. Growth Des., 20 (2020) 824–831.

[23] H. Liu, Y.J. Chen, G.H. Tian, Z.Y. Ren, C.G. Tian, H.G. Fu, Visible-light-induced self-cleaning property of $Bi_2Ti_2O_7$-TiO_2 composite nanowire arrays, Langmuir, 31 (2015) 5962–5969.

[24] B.T. Liu, Q.H. Mo, J.L. Zhu, Z.P. Hou, L.L. Peng, Y.J. Tu, Q.Y. Wang, Synthesis of Fe and N Co-doped $Bi_2Ti_2O_7$ nanofiber with enhanced photocatalytic activity under visible light irradiation, Nanoscale Res. Lett., 11 (2016) 391, doi: 10.1186/s11671-016-1610-7.
[25] P.J. Li, C.Y. Jiang, C.S. Feng, Y.P. Wang, Effects of different exposed-facets on photocatalytic activity of BiOBr/$Bi_2Ti_2O_7$ heterostructure and mechanism analysis, Mater. Chem. Phys., 252 (2020) 123426, doi: 10.1016/j.matchemphys.2020.123426.
[26] Z.Y. Zhang, C.Y. Jiang, P. Du, Y.P. Wang, Synthesis and characterization of $Bi_2Ti_2O_7$/TiO_2 heterojunction by glycerol-assisted alcoholthermal method, Ceram. Int., 41 (2015) 3932–3939.
[27] J.H. Li, M.S. Han, Y. Guo, F. Wang, L.J. Meng, D.J. Mao, S.S. Ding, C. Sun, Hydrothermal synthesis of novel flower-like $BiVO_4$/$Bi_2Ti_2O_7$ with superior photocatalytic activity toward tetracycline removal, Appl. Catal., A, 524 (2016) 105–114.
[28] K. Qian, L. Xia, W. Wei, L.L. Chen, Z.F. Jiang, J.J. Jing, J.M. Xie, Construction of $Bi_2Ti_2O_7$/$Bi_4Ti_3O_{12}$ composites with enhanced visible light photocatalytic activity, Mater. Lett., 206 (2017) 245–248.
[29] N. Li, M.L. Shi, Y. Xin, W. Zhang, J.N. Qin, K. Zhang, H.Q. Lv, M.Z. Yuan, C.Y. Wang, Oxygen vacancies-modified S-scheme $Bi_2Ti_2O_7$/$CaTiO_3$ heterojunction for highly efficient photocatalytic NO removal under visible light, J. Environ. Chem. Eng., 10 (2022) 107420, doi: 10.1016/j.jece.2022.107420.
[30] Y.X. Xu, D.F. Lin, X.P. Liu, Y.J. Luo, H. Xue, B.Q. Huang, Q.H. Chen, Q.R. Qian, Electrospun BiOCl/$Bi_2Ti_2O_7$ nanorod heterostructures with enhanced solar light efficiency in the photocatalytic degradation of tetracycline hydrochloride, ChemCatChem, 10 (2018) 2496–2504.
[31] C.L. Mayfield, M.N. Huda, Free energy landscape approach to aid pure phase synthesis of transition metal (X = Cr,Mn and Fe) doped bismuthtitanate ($Bi_2Ti_2O_7$), J. Cryst. Growth, 444 (2016) 46–54.
[32] F.F. Li, X. Liu, J.X. Zhao, L. Liu, S. He, D.H. Bao, Red-orange photoluminescence and dielectric relaxation of Eu^{3+}-doped $Bi_2Ti_2O_7$ pyrochlore structure thin films, Mater. Chem. Phys., 162 (2015) 801–806.
[33] Y.K. Cun, Z.W. Yang, J. Li, B. Shao, J.Z. Yang, Y.D. Wang, J.B. Qiu, Z.G. Song, Enhanced upconversion emission of three dimensionally ordered macroporous films $Bi_2Ti_2O_7$:Er^{3+}, Yb^{3+} with silica shell, Ceram. Int., 41 (2015) 11770–11775.
[34] L.B. Jiang, J.J. Yang, S.Y. Zhou, H.B. Yu, J. Liang, W. Chu, H. Li, H. Wang, Z.B. Wu, X.Z. Yuan, Strategies to extend near-infrared light harvest of polymer carbon nitride photocatalysts, Coord. Chem. Rev., 439 (2021) 213947, doi: 10.1016/j.ccr.2021.213947.
[35] H.M. Huang, L.B. Jiang, J.J. Yang, S.Y. Zhou, X.Z. Yuan, J. Liang, H. Wang, H. Wang, Y.Q. Bu, Hui Li, Synthesis and modification of ultrathin g-C_3N_4 for photocatalytic energy and environmental applications, Renewable Sustainable Energy Rev., 173 (2023) 113110, doi: 10.1016/j.rser.2022.113110.
[36] J. Mei, D.P. Zhang, N. Li, M.X. Zhang, X.Y. Gu, S.C. Miao, S.H. Cui, J. Yang, The synthesis of Ag_3PO_4/g-C_3N_4 nanocomposites and the application in the photocatalytic degradation of bisphenol A under visible light irradiation, J. Alloys Compd., 749 (2018) 715–723.
[37] J.J. Lu, X.G. Tang, W.M. Zhong, Y.P. Jiang, Q.X. Liu, Resistive switching characteristics of interfacial device based on $Bi_2Ti_2O_7$ film, Surf. Interfaces, 37 (2023) 102655, doi: 10.1016/j.surfin.2023.102655.
[38] M. Musso, S. Veiga, A.D. Leon, A. Quevedo, J. Bussi, Characterization and application of a bismuth titanate $Bi_2Ti_2O_7$ synthetized through a solvothermal route for glycerol photooxidation and photoreforming, Mater. Lett., 330 (2023) 133346, doi: 10.1016/j.matlet.2022.133346.
[39] Z.W. Qiao, W.Q. Chu, H. Zhou, C. Peng, Z.Z. Guan, J. Wu, S. Yoriya, P. He, H. Zhang, Y.F. Qi, Construction of Z scheme S-g-C_3N_4/Bi_5O_7I photocatalysts for enhanced photocatalytic removal of Hg^0 and carrier separation, Sci. Total Environ., 872 (2023) 162309, doi: 10.1016/j.scitotenv.2023.162309.
[40] D.Y. Yang, Y. Wang, J. Zhao, J.D. Dai, Y.S. Yan, L. Chen, J. Ye, Strong coupling of super-hydrophilic and vacancy-rich g-C_3N_4 and LDH heterostructure for wastewater purification: adsorption-driven oxidation, J. Colloid Interface Sci., 639 (2023) 355–368.
[41] S.M. Wang, D.L. Li, C. Sun, S.G. Yang, Y. Guan, H. He, Synthesis and characterization of g-C_3N_4/Ag_3VO_4 composites with significantly enhanced visible-light photocatalytic activity for triphenylmethane dye degradation, Appl. Catal., B, 144 (2014) 885–892.
[42] B. Hu, F.P. Cai, T.J. Chen, M.S. Fan, C.J. Song, X. Yan, W.D. Shi, Hydrothermal synthesis g-C_3N_4/nano-$InVO_4$ nanocomposites and enhanced photocatalytic activity for hydrogen production under visible light irradiation, ACS Appl. Mater. Interfaces, 7 (2015) 18247–18256.
[43] W.X. Wang, Z. Li, K.L. Wu, G.D. Dai, Q.P. Chen, L.H. Zhou, J.X. Zheng, L. Ma, G.Y. Li, W.J. Wang, T.C. An, Novel Ag-bridged dual Z-scheme g-C_3N_4/BiOI/AgI plasmonic heterojunction: exceptional photocatalytic activity towards tetracycline and the mechanism insight, J. Environ. Sci., 131 (2023) 123–140.
[44] R.L. Wei, H. Wang, L.B. Jiang, J.J. Yang, W.Q. Li, X.Z. Yuan, H. Wang, J. Liang, Y.N. Chen, Y.Q. Bu, Molecular self-assembled synthesis of highly dispersed Co single-atom coordinated 2-methylimidazole modified carbon nitride for peroxymonosulfate activation, Chem. Eng. J., 471 (2023) 144494–144506.
[45] D.K. Gorai, S.K. Kuila, A. Oraon, A. Kumar, M. Suthar, R. Mitra, K. Biswas, P.K. Roy, M.I. Ahmad, T.K. Kundu, A facile and green synthesis of Mn and P functionalized graphitic carbon nitride nanosheets for spintronics devices and enhanced photocatalytic performance under visible-light, J. Colloid Interface Sci., 644 (2023) 397–414.
[46] X.Y. Li, H.X. Mai, N. Cox, J.L. Lu, X.M. Wen, D.H. Chen, R.A. Caruso, Sb-substituted $Cs_2AgBiBr_6$/g-C_3N_4 composite for photocatalytic C(sp^3)-H bond activation in toluene, Chem. Mater., 35 (2023) 3105–3114.
[47] X.J. Zhou, G. Zhang, C.L. Shao, X.H. Li, X. Jiang, Y.C. Liu, Fabrication of g-C_3N_4/SiO_2-Au composite nanofibers with enhanced visible photocatalytic activity, Ceram. Int., 43 (2017) 15699–15707.
[48] C.Y. Jin, C.H. Xu, W.X. Chang, X.Y. Ma, X.Y. Hu, E.Z. Liu, J. Fan, Bimetallic phosphide NiCoP anchored g-C_3N_4 nanosheets for efficient photocatalytic H_2 evolution, J. Alloys Compd., 803 (2019) 205–215.
[49] J. Ren, Y.Y. Chai, Q.Q. Liu, L. Zhang, W.L. Dai, Intercorrelated Ag_3PO_4 nanoparticles decorated with graphic carbon nitride: enhanced stability and photocatalytic activities for water treatment, Appl. Surf. Sci., 403 (2017) 177–186.
[50] Q.Y. Rong, D.P. Zhang, Y. Li, Z.X. Zha, X.X. Geng, S.H. Cui, J. Yang, Synthesis of Bi_2MoO_6/$Bi_2Ti_2O_7$ Z-scheme heterojunction as efficient visible-light photocatalyst for the glycolic acid degradation, J. Nanosci. Nanotechnol., 19 (2019) 7635–7644.
[51] J.H. Yi, X.J. Yuan, H.J. Wang, H. Yu, F. Peng, Preparation of $Bi_2Ti_2O_7$/TiO_2 nanocomposites and their photocatalytic performance under visible light irradiation, Mater. Des., 86 (2015) 152–155.
[52] J.L. Zhang, H. Liu, Z. Ma, Flower-like Ag_2O/Bi_2MoO_6 p-n heterojunction with enhanced photocatalytic activity under visible light irradiation, J. Mol. Catal. A: Chem., 424 (2016) 37–44.
[53] H.F. Shi, H.Q. Tan, W.B. Zhu, Z.C. Sun, Y.J. Ma, E.B. Wang, Electrospun Cr-doped $Bi_4Ti_3O_{12}$/$Bi_2Ti_2O_7$ heterostructure fibers with enhanced visible-light photocatalytic properties, J. Mater. Chem. A, 3 (2015) 6586–6591.
[54] Q.H. Zhu, R. Hailili, Y. Xin, Y.T. Zhou, Y. Huang, X.Z. Pang, K. Zhang, P.K.J. Robertson, D.W. Bahnemann, C.Y. Wang, Efficient full spectrum responsive photocatalytic NO conversion at $Bi_2Ti_2O_7$: co-effect of plasmonic Bi and oxygen vacancies, Appl. Catal. B: Environ., 319 (2022) 121888, doi: 10.1016/j.apcatb.2022.121888.
[55] Z.H. Zhao, Y. Wang, Q. Yu, X.C. Lin, X.W. Xu, J. Zhang, H.J. Lu, X.X. Chen, D.P. Zhang, Construction of $AgBiO_3$/g-C_3N_4 nanocomposites with enhanced photocatalytic activity and their application in the degradation of bisphenol A, Desal. Water Treat., 227 (2021) 228–237.

[56] V. Vinesh, M. Preeyanghaa, T.R. Naveen Kumar, M. Ashokkumar, C.L. Bianchi, B. Neppolian, Revealing the stability of $CuWO_4$/g-C_3N_4 nanocomposite for photocatalytic tetracycline degradation from the aqueous environment and DFT analysis, Environ. Res., 207 (2022) 112112, doi: 10.1016/j.envres.2021.112112.

[57] H. Sudrajat, S. Babel, A new, cost-effective solar photoactive system N-ZnO@polyester fabric for degradation of recalcitrant compound in a continuous flow reactor, Mater. Res. Bull., 83 (2016) 369–378.

[58] D.P. Zhang, S.H. Cui, J. Yang, Preparation of Ag_2O/g-C_3N_4/Fe_3O_4 composites and the application in the photocatalytic degradation of Rhodamine B under visible light, J. Alloys Compd., 708 (2017) 1141–1149.

[59] Y. Zhong, J.Q. Chang, C.H. Hu, J.F. Zhou, Fabrication of novel heterostructured catalyst Ag@AgCl/$Bi_2Ti_2O_7$ and its excellent visible light photocatalytic performance, J. Mol. Struct., 1222 (2020) 128938, doi: 10.1016/j.molstruc.2020.128938.

[60] J.H. Lai, P. Xiao, Y.F. Li, S.H. Cui, J. Yang, H.Z. Lian, Visible light and iodate/iodide mediated degradation of bisphenol A by self-assembly 3D hierarchical $BiOIO_3$/Bi_5O_7I Z-scheme heterojunction: intermediates identification, radical mechanism and DFT calculation, J. Hazard. Mater., 448 (2023) 130908, doi: 10.1016/j.jhazmat.2023.130908.

[61] X.Y. Gu, J. Mei, J.H. Lai, S.Y. Lv, J. Yang, S.H. Cui, S. Chen, Synthesis of Z-Scheme heterojunction $ZnNb_2O_6$/g-C_3N_4 nanocomposite as a high efficient photo-catalyst for the degradation of 2,4-DCP under simulated sunlight, Mater. Res. Bull., 130 (2020) 110939, doi: 10.1016/j.materresbull.2020.110939.

[62] J.H. Lai, X.Y. Jiang, M. Zhao, S.H. Cui, J. Yang, Y.F. Li, Thickness-dependent layered $BiOIO_3$ modified with carbon quantum dots for photodegradation of bisphenol A: mechanism, pathways and DFT calculation, Appl. Catal., B, 298 (2021) 120622, doi: 10.1016/j.apcatb.2021.120622.